INT. J. NUM. METH. HEAT FLUID FLOW, VOL 2, 537–553 (1992)

A STUDY OF THE HYDROELASTIC STABILITY OF A COMPLIANT PANEL USING NUMERICAL METHODS

ANTHONY D. LUCEY AND PETER W. CARPENTER

Department of Engineering, University of Warwick, Coventry, CV4 7AL, UK

ABSTRACT

A numerical method is developed which can simulate the interaction between a finite compliant panel and an unsteady potential flow. A boundary-element technique yields the flow solution whilst finite-differences are used to solve the wall dynamics; these are then coupled to generate a fully interactive wall/flow system. Thus, the evolution of any wall disturbance can be followed. Parallel computing is appropriately employed and a stability investigation of a realistic compliant panel is carried out. Three-dimensional flexural waves are found below a critical flow speed whilst beyond this threshold, essentially two-dimensional unstable divergence waves are found. The form of divergence shows good agreement with that seen in experimental studies. The versatility of this new method will permit the investigation of a wide variety of single- and multi-panel configurations subject to different forms of excitation.

KEY WORDS Compliant wall Hydroelastic stability Boundary-element method CFD Parallel computing

INTRODUCTION

The interaction between a boundary-layer flow and a passive compliant wall can produce a delay in laminar-to-turbulent transition. This has been shown theoretically by Carpenter and Garrad[1], Yeo[2,3] and Carpenter and Morris[4]. The successful experimental work of Daniel *et al.*[5], Gaster[6] and Willis[7] demonstrated that wall compliance reduced the growth rates of the Tollmien–Schlichting (T–S) waves thereby extending the linear part of the transition length. This effect can be exploited to yield valuable reductions to the skin-friction drag of marine vehicles. Recent work on compliant walls optimised for transition delay[8,9] suggest that a 60% reduction to the skin-friction drag of a small submersible is achievable. The key to designing useful compliant walls lies in giving proper consideration to all of the instabilities which might exist within the wall/flow system. The introduction of compliance serves to attenuate the T–S waves but renders the system susceptible to hydroelastic instabilities. Lucey *et al.*[10] have shown one of these wall-based instabilities could have accounted for the dramatic breakdown of the flow over the softer compliant walls recorded in the aforementioned experimental work.

The two most important hydroelastic instabilities, which can be considered to be wall-based, are travelling-wave flutter (TWF) and divergence. The mechanisms underlying these instabilities (and that of the T–S waves) are discussed in Carpenter[11]. For convenience a brief description is included here. TWF is a conventional wall wave which may grow as it travels downstream due to an irreversible energy transfer from the fluid flow into the wall. It is the presence of a boundary layer which introduces this type of energy transfer by effectively applying a phase shift to the pressure forces as they are transmitted to the wall from the outer potential flow. Like the T–S waves, this is a *convective* instability—it grows as it travels downstream from some initial

0961–5539/92/060537–17$2.00

Received November 1991

disturbance. Divergence instability is essentially a result of the interaction between conservative wall and fluid forces, the latter obtaining from disturbances to the flow outside of the boundary layer. In simple terms, then, when the hydrodynamic stiffness due to a wall disturbance exceeds the structural restorative forces in the wall, divergence ensues. Experimental evidence of divergence[12–14] shows it to be a slow downstream-travelling wave. However, a two-dimensional analysis of Carpenter and Garrad[15] has shown that this wave has zero group velocity. This implies that it is an *absolute* instability which would evidence growth at all locations of the compliant wall. Confirmation of this character, for the two-dimensional study, has been provided by the numerical simulations of Lucey and Carpenter[16] which show the spread of the instability in both upstream and downstream directions from a location of initial excitation. Given this absolute character, it is essential that compliant walls are designed to be divergence free. The present paper sets out to further our understanding of divergence instability. In particular, we use suitable numerical methods to study the divergence of a finite compliant panel for which the three-dimensionality of disturbances and panel-edge effects are expected to be important.

A method is therefore developed which can simulate the response of a finite compliant panel to an unsteady incompressible potential flow. A boundary-element method provides the flow solution which is then coupled to a finite-difference representation of wall mechanics. The wall/flow system is solved globally; this approach is essential given the absolute nature of divergence instability. A semi-implicit numerical scheme is employed for the time-stepping so that numerical phase shifts are minimized—the presence of this type of phase shift could be manifest as an artificial transfer of energy between the wall and flow. In effect, the philosophy follows that employed in the two-dimensional simulations of Lucey and Carpenter[16]. However, the three-dimensional work presented here is computationally far more demanding. To meet these needs, parallel computing is used with the solution algorithms tailored to exploit the architecture of the distributed-array processor. The resulting computer code offers a versatile means to follow the development of the wall/flow system and to determine the onset flow speeds of divergence instability for a variety of compliant-panel configurations. In contrast to a classical approach to the hydroelastic analysis of flexible panels[17–20], the disturbance form is completely arbitrary. Moreover, the present method allows different means of initial excitation of the wall to be investigated.

The assumption of purely potential flow is suitable for the prediction of divergence instability but precludes the existence of TWF. Nevertheless, the numerical simulations are able to model the flexural waves that support TWF and which are modified both by the hydrodynamic forces that originate beyond the boundary layer, and by the presence of panel edges. The present model captures the primary response of the compliant wall; future work can build on this model most particularly through the incorporation of a boundary layer. In all of the following a plate-spring model of a single compliant panel is used. It should be remarked that the methodology is applicable to other types of compliant wall provided that a suitable wall solution is available. Additionally the present work may easily be extended to model the arrays of compliant panels that will undoubtedly be used in practical applications.

MATHEMATICAL MODEL

The type of wall used in the present model was developed in Reference 1 to model the coatings used in Kramer's[21] pioneering experimental work. It consists of an isotropic flexible plate supported by a uniformly-distributed spring foundation and may include conventional damping. In-plane forces are neglected. This type of compliant-wall structure is illustrated in *Figure 1* along with the co-ordinate system used in the following work and the direction of flow. The

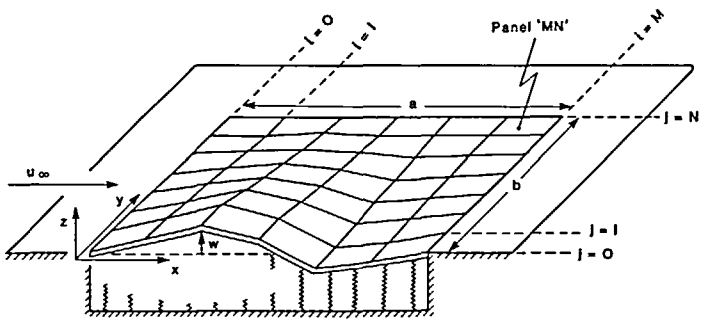

Figure 1 Schematic of the compliant panel showing the discretization into panel-elements

equation of motion, for vertical deflections of the wall, $w(x, y, t)$, is:

$$\rho_m h\ddot{w} + d\dot{w} + [B\nabla^2\nabla^2 + K_E]w = -\delta p(\ddot{w}, \dot{w}, w) \tag{1}$$

where ρ_m and h are the density and thickness of the flexible plate, d is a damping coefficient and K_E is an equivalent spring stiffness which combines the effects of the foundation springs and body forces. The hydrodynamic pressure due to the wall disturbance is given by δp. Dot notation indicates differentiation with respect to time. The plate flexural rigidity, B, and the biharmonic operator are, respectively, defined by:

$$B = \frac{Eh^3}{12(1-\nu^2)}, \quad [\nabla^2\nabla^2] \equiv \left[\frac{\partial^4}{\partial x^4} + 2\frac{\partial^4}{\partial x^2 \partial y^2} + \frac{\partial^4}{\partial y^4}\right]$$

where E and ν are the elastic modulus and Poisson ratio of the plate. Other types of compliant wall can be modelled by choosing an appropriate differential operator (in (1)) for the wall restorative stiffness; these forms are discussed in Dowell[22].

To evaluate the driving hydrodynamic pressure perturbations seen on the right-hand side of (1), it is necessary to solve the Laplace equation subject to the no-flux condition at the wall/fluid interface. Previous methods of solution[18–20] have represented the surface deformation as a collection of orthogonal modes in order to render the problem tractable. For a finite panel with hinged edges, Lucey and Carpenter[23] used the simple form:

$$w(x, y, t) = \exp(i\omega t) \sum_{k=1}^{\infty} \sum_{l=1}^{\infty} A_{kl} \sin(k\pi x/a) \sin(l\pi y/b) \tag{2}$$

where a and b are the panel dimensions, ω is the complex angular frequency and A_{kl} is the (complex) intensity of the mode with numbers $\{k, l\}$. The flow solution can be found, for example, using thin-aerofoil theory and the system problem, represented by (1), solved using a Galerkin method to yield global predictions of the wall behaviour. It should be noted that in the practical implementation of this type of approach, the Fourier expansion of the wall disturbance is severely truncated or restricted to a, usually small, finite number of selected modes.

NUMERICAL MODEL

To proceed with the numerical modelling of the system, the flexible surface is discretized into an array of panel-elements as shown in *Figure 1*; the mesh-line numbering and panel notation used below are included in this Figure. Mass-points are located at the intersection of mesh lines for the finite-difference scheme representation of the wall mechanics.

Wall mechanics

A pair of suitable basis equations, together with the finite-difference form of (1), for an implicit solution are written as:

$$w_{ij}^{t+\delta t} = w_{ij}^{t} + (\delta t/2)(\dot{w}_{ij}^{t} + \dot{w}_{ij}^{t+\delta t}) \tag{3a}$$

$$\dot{w}_{ij}^{t+\delta t} = \dot{w}_{ij}^{t} + (\delta t/2)(\ddot{w}_{ij}^{t} + \ddot{w}_{ij}^{t+\delta t}) \tag{3b}$$

$$\ddot{w}_{ij}^{t+\delta t} = -\frac{1}{\rho_m h}\{d\dot{w}_{ij}^{t+\delta t} + [B\nabla^2\nabla^2 + K_E]w_{ij}^{t+\delta t} + \delta p_{ij}(w^{t+\delta t}, \dot{w}^{t+\delta t}, \ddot{w}^{t+\delta t})\} \tag{3c}$$

Structural coupling of mass points occurs through the biharmonic operator which, using centred differences, is given by:

$$\begin{aligned}[\nabla^2\nabla^2]w_{ij} = {} & (6/\delta x^4 + 8/(\delta x\delta y)^2 + 6/\delta y^4)w_{ij} + \\ & 4(1/\delta x^4 + 1/(\delta x\delta y)^2)(w_{i-1,j} + w_{i+1,j}) + \\ & 4(1/\delta y^4 + 1/(\delta x\delta y)^2)(w_{i,j-1} + w_{i,j+1}) - \\ & (1/\delta x^4)(w_{i-2,j} + w_{i+2,j}) - (1/\delta y^4)(w_{i,j-2} + w_{i,j+2}) + \\ & (2/(\delta x\delta y)^2)(w_{i-1,j-1} + w_{i+1,j-1} + w_{i-1,j+1} + w_{i+1,j+1})\end{aligned}$$

where δx and δy are the mesh-line spacings. Here, for convenience, we have assumed a uniform mesh. The hinged-edges of the compliant panel are modelled by enforcing the conditions of zero deflection and zero turning moment along the edges. In discretized form, then:

$$w_{0,j} = w_{i,0} = w_{M,j} = w_{i,N} = 0$$

and

$$w_{-1,j} = 2(1 + \nu/\kappa^2)w_{0,j} - (\nu/\kappa^2)(w_{0,j-1} + w_{0,j+1}) - w_{1,j} \qquad \text{for } j = -1, 0, 1, \ldots, N, N+1$$

$$w_{i,-1} = 2(1 + \nu\kappa^2)w_{i,0} - (\nu\kappa^2)(w_{i-1,0} + w_{i+1,0}) - w_{i,1} \qquad \text{for } i = -1, 0, 1, \ldots, M, M+1$$

$$w_{M+1,j} = 2(1 + \nu/\kappa^2)w_{M,j} - (\nu/\kappa^2)(w_{M,j-1} + w_{M,j+1}) - w_{M-1,j} \qquad \text{for } j = -1, 0, 1, \ldots, N, N+1$$

$$w_{i,N+1} = 2(1 + \nu\kappa^2)w_{i,N} - (\nu\kappa^2)(w_{i-1,N} + w_{i+1,N}) - w_{i,N-1} \qquad \text{for } i = -1, 0, 1, \ldots, M, M+1$$

where $\kappa = \delta x^2/\delta y^2$. The above forms of the biharmonic operator and the edge conditions necessitate the introduction of a set of 'dummy' points located around the compliant panel and defined by the mesh lines, $i = -1, j = -1, i = M + 1$ and $j = N + 1$.

For the compliant-panel motion in the absence of a fluid, then $\delta p_{ij} = 0$ and (3) can be solved using Gauss–Seidel sweeps to track the free-wave behaviour of the panel after an initial perturbation from its equilibrium position in the plane $z = 0$. The iteration procedure for each time step is complete when convergence has been reached for all of w_{ij}, $\dot{w}_{ij}$ and $\ddot{w}_{ij}$.

Fluid mechanics

To model the interactive wall/flow system, a suitable form for the perturbation pressure, δp_{ij}, needs to be found. The $M \times N$ array of panel-elements, seen in *Figure 1*, is used to construct a boundary-element solution. Following the methods of Hess and Smith[24], each panel-element is assigned a source strength, σ_{ij}, the value of which is determined by applying the condition of zero flux at the surface. This boundary condition can be written as:

$$2\pi\sigma_{ij} + \sum_{\substack{m=1 \\ m\neq i}}^{M}\sum_{\substack{n=1 \\ n\neq j}}^{N} \sigma_{mn} I_{ijmn} + \mathbf{U}_\infty \cdot \mathbf{n}_{ij} = u_{ij}^{p} \tag{4}$$

where the source-strength influence coefficients are given by the surface integral:

$$I_{ijmn} = \iint_{\substack{\text{panel} \\ mn}} \frac{\partial}{\partial n_{ij}}\left(\frac{1}{|\mathbf{r}_{ij} - \mathbf{r}_{mn}|}\right) \mathrm{d}S$$

In the above equations, $\mathbf{r}_{ij}$ is the vector describing the control point (in this application, the centre) of panel-element ij, $\mathbf{n}_{ij}$ is the unit vector normal to panel-element ij and u_{ij}^{p} is its velocity in this direction. The vector $\mathbf{r}_{mn}$ varies through all surface locations of the panel-element mn for the integration. For a given surface deformation and surface-velocity distribution, the linear system of equations (defined by (4)) can be solved to yield the source-sink strengths. Thereafter, the values of perturbation-velocity potential at each panel-element control point can be evaluated.

The above method is able to cope with non-linear wall disturbances; but, the full non-linear version has only been computer coded for the case of static deflections. In fact, we are interested in the dynamic behaviour of the wall/flow system; the changing geometry of the wall with time means that at each iteration of each time-step, the influence coefficients might need to be re-calculated. This computationally expensive procedure has led us to develop a faster method of flow solution but which is restricted to small (i.e. linear) disturbances of the compliant wall. This approximate method stipulates that the influence coefficients remain in the undisturbed plane, $z = 0$, and that the source-sink strengths of a particular panel-element are solely dependent upon its deflection. The second condition decouples (4), leading to the simple determination of source strengths:

$$\sigma_{ij}(w, \dot{w}) = \frac{1}{2\pi}(U_\infty \alpha_{ij}(w) + u_{ij}^{v}(\dot{w})) \tag{5}$$

where α_{ij} is the panel-element angle of slope relative to the x-axis and u_{ij}^{v} is the vertical velocity of the panel control point. The accuracy of this approximate method has been improved by incorporating a linear variation to the steady part of the source strength seen in (5). Thus, solutions for the velocity-perturbation potential and the x-direction tangential velocity at the control points take the forms:

$$\Phi_{ij} = \sum_{m=1}^{M}\sum_{n=1}^{N} \sigma_{mn} I_{ijmn}^{\Phi} \qquad u_{ij} = \sum_{m=1}^{M}\sum_{n=1}^{N} \{\sigma_{mn} I_{ijmn}^{U0} + \lambda_{mn} I_{ijmn}^{U1}\} \tag{6a,b}$$

where λ_{mn} is the coefficient of the linear-variation of source strength on panel-element mn and I_{ijnm}^{Φ}, I_{ijmn}^{U0} and I_{ijnm}^{U1} are sets of geometry-dependent influence coefficients. It is emphasized that all of these influence coefficients are evaluated for the compliant panel in the undisturbed position and remain unchanged throughout the motion of the wall/flow interface. Thus, they need only be calculated once—before the finite-difference solution for the system is initiated. This linear variant of the boundary-element method has been tested against the non-linear method described above for a static deflection and been shown to give acceptable agreement provided that disturbance amplitudes remain within 1% of the wavelength of a sinusoidal-type disturbance.

The pressure perturbations at the panel-element control points can now be found using a discretized form of the linearized unsteady Bernoulli equation:

$$\delta p_{ij} = -\rho U_\infty u_{ij} - \rho \frac{\partial \Phi_{ij}}{\partial t} \tag{7}$$

where ρ is the fluid density. It can be seen that upon substituting for u_{ij} and Φ_{ij} using (6) (and noting the functional dependence of σ_{ij} in (5)), the pressure perturbation takes the form:

$$\delta p_{ij}(\ddot{w}, \dot{w}, w) = \delta p_{U2_{ij}}(\ddot{w}) + \delta p_{U1_{ij}}(\dot{w}) + \delta p_{S^2{}_{ij}}(\dot{w}) + \delta p_{S1_{ij}}(w) \tag{8}$$

This decomposition of the unsteady pressure illustrates the presence of hydrodynamic inertia ($\ddot{w}$-dependent terms), damping ($\dot{w}$-dependent terms) and stiffness (w-dependent terms) in the fluid forcing. The absence of suffices in the arguments above indicates that the variable value at every mass-point is required for the function evaluation.

Solution of the coupled wall/flow system

The wall and flow solutions are coupled by introducing the pressure perturbations, (8), into the finite-difference equations which describe the wall motion. The above perturbation pressures have been evaluated at the panel-element control points; simple averaging of the values at the four panel-elements surrounding a mass-point yields the appropriate value at the mass point. Having carried out this averaging and written the form of $\delta p_{U2}(\ddot{w})$ explicitly (using (5) and (6a)), the acceleration equation, (3c), becomes:

$$\ddot{w}_{ij}^{t+\delta t} + \frac{\rho}{2\pi\rho_m h}\sum_{m=1}^{M-1}\sum_{n=1}^{N-1}\left\{\frac{(I^{\Phi}_{ijmn} + I^{\Phi}_{i+1,jmn} + I^{\Phi}_{i,j+1,mn} + I^{\Phi}_{i+1,j+1,mn})}{4}\times \frac{(\ddot{w}^{t+\delta t}_{m-1,n-1} + \ddot{w}^{t+\delta t}_{m,n-1} + \ddot{w}^{t+\delta t}_{m-1,n} + \ddot{w}^{t+\delta t}_{m,n})}{4}\right\} = F_{ij}(w^{t+\delta t}, \dot{w}^{t+\delta t}) \tag{9}$$

where:

$$F_{ij}(w^{t+\delta t}, \dot{w}^{t+\delta t}) = -\frac{1}{\rho_m h}\{d\dot{w}_{ij}^{t+\delta t})[B\nabla^2\nabla^2 + K_E]w_{ij}^{t+\delta t} + \delta p_{U1_{ij}}(\dot{w}^{t+\delta t}) + \delta p_{S2_{ij}}(\dot{w}^{t+\delta t}) + \delta p_{S1_{ij}}(w^{t+\delta t})\}$$

This represents a linear system of equations, order $(M-1)\times(N-1)$, for the unknowns, $\ddot{w}_{ij}^{t+\delta t}$ which can be written in the form:

$$G_{ijmn}\ddot{w}_{mn}^{t+\delta t} = F_{ij}(w^{t+\delta t}, \dot{w}^{t+\delta t}) \tag{10}$$

where the matrix G_{ijmn} (i,m: $1\rightarrow(M-1)$ and j,n: $1\rightarrow(N-1)$) has elements comprising the influence coefficients I^{Φ}_{ijmn} which are solely geometry dependent and, in the linear boundary-element method, remain unchanged throughout the evolution of wall disturbances. The matrix can thus be assembled, inverted and stored before the solution procedure is initiated. Once the wall/system solution is underway the inverted matrix can be invoked to solve (10) at the appropriate point of the iteration cycle which continues to be represented by (3). In the present method, it has been found sufficient to use the mass-point deflections and velocities at the start of the time-step when evaluating the pressure terms in the column vector, F_{ij}, of (10). This yields substantial savings in computational time without noticeably compromising the accuracy of the solution; for this reason, we describe the solution procedure as semi-implicit.

APPLICATION OF PARALLEL COMPUTING

The methods described above are ideally suited to parallel processing. The array of panel elements seen in *Figure 1* is mapped onto the basic array of a distributed-array processor (DAP). The parallel computations were carried out on a SUN4/AMT DAP510. This is a SIMD mini-supercomputer system. Thus, a set of influence coefficients associated with a particular panel-element, *ij*, due to the influence of all the remaining panel-elements can be calculated in a single operation. Of greater importance is the repeated calculation, as the wall deflection evolves, of all of the source strengths, (5), and the evaluation of velocity-perturbation potential,

(6a), and tangential perturbation velocity, (6b), at a particular panel; these, too, reduce to single operations. In addition, the execution of the finite-difference solution for the wall/flow system, can be substantially expedited. In each of (3a) and (3b), concurrent calculation at every mass-point is carried out rather than sweeping through the array of panel-elements. These equations are naturally two-dimensional whereas (9) and (10) are essentially four-dimensional owing to the presence of expressions such as I^{Φ}_{ijmn}. For large mesh sizes this leads to enormous storage requirements both for all three sets of influence coefficients and the inverted matrix, G^{-1}_{ijmn}, required to solve (10). We have therefore sought to couch these parts of the procedure in a two-dimensional form appropriate to the DAP and reduce memory requirements.

Reduced memory requirements for influence coefficients

In our applications we choose to use uniform discretizations of the compliant panel that give arrays of identical panel elements. This approach is adopted because the wall motion is allowed to evolve freely; to use mesh-refinement techniques in particular regions would require knowledge of the wall behaviour in advance. The use of a single size of panel-element allows symmetries of the influence-coefficient matrices to be exploited.

The array of panel-elements, size $M \times N$, is mapped onto the basic array of the DAP, and taken to be located in A(„ 1, 1) as shown in the schematic (*Figure 2*). A discretization comprising identically-sized panel elements but having an array of dimensions $(2M - 1) \times (2N - 1)$ is then set up. This occupies four basic arrays of the DAP, again as shown in *Figure 2*. A key panel-element, located at A(M, N, 1, 1) is chosen and the coefficients for this one panel-element obtaining from the influence of all of the $(2M - 1) \times (2N - 1)$ panel-elements evaluated and stored. This larger single, two-dimensional, array of influence coefficients then includes sets of influence coefficients appropriate to every panel-element existing on the actual compliant panel. The set of influence coefficients relevant to a particular panel-element, *ij*, can be obtained by shifting the larger array so that the key panel-element is coincident with the particular panel-element and selecting the array elements that now fall within the boundaries of the array of actual panel-elements; this process is illustrated in *Figure 2b*. Using this technique, each four-dimensional array of size $M \times N \times M \times N$ is reduced to a two-dimensional array of size $(2M - 1) \times (2N - 1)$. The

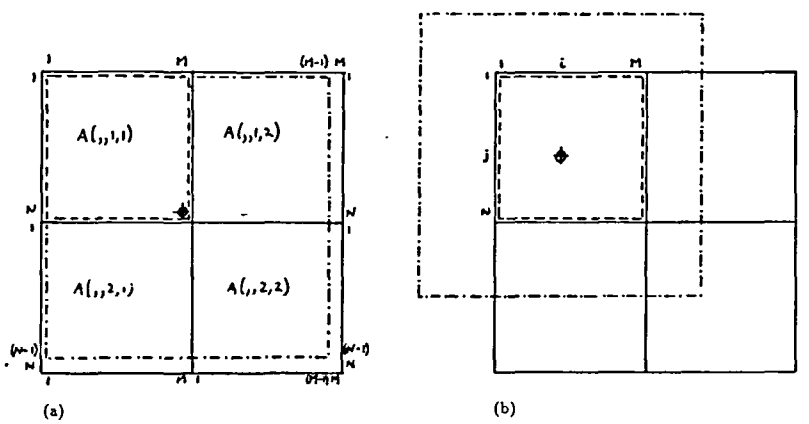

Figure 2 Schematic of the DAP processor arrays used in the calculation of influence coefficients. (a) Set-up for calculation of all influence coefficients and selection of influence coefficients for the particular panel-element, *MN*. (b) Shifted large array for the selection of influence coefficients for panel-element, *ij*. ⊕, Key panel-element; ––, array containing actual panel elements; –·–, large array containing all influence coefficients

availability on the DAP of implicit functions such as array-shift and 'equivalence' (identifying the four basic arrays with the larger array seen in *Figure 2a*) makes the implementation of this technique on the DAP relatively simple.

Alternative solution of the acceleration equation

For large mesh sizes, it is desirable to avoid the storage (or repeated reading-in) of the matrix G^{-1}_{ijmn} required to solve (10) at every iteration of each time-step. What follows is an alternative method to cope with this stage of the iteration cycle. The inertial side of the system of equations, (9), is first simplified by partial decoupling. An 'internal' mesh is used to generate the hydrodynamic inertia term, $\delta p_{U2}(\ddot{w})$, in (8). Relative to the mesh seen in *Figure 1*, this new mesh is defined by the lines: $i = 1/2, 3/2, \ldots, (M - 1/2)$ with $j = 1/2, 3/2, \ldots, (N - 1/2)$. Evidently, the ensuing panel-elements are of identical size and relative position to the original set. There is, therefore, no need to calculate a new set of the appropriate influence coefficients, I^{Φ}_{ijmn}. This internal set of panel elements has its control points coincident with the mass points and thus (9) takes the simpler form:

$$\ddot{w}^{t+\delta t}_{ij} + \frac{\rho}{2\pi\rho_m h} \sum_{m=1}^{M-1} \sum_{n=1}^{N-1} I^{\Phi}_{ijmn} \ddot{w}^{t+\delta t}_{m,n} = F_{ij}(w^{t+\delta t}, \dot{w}^{t+\delta t}) \tag{11}$$

From a physical consideration of the hydrodynamic inertia, it is known that the dominant coefficients of the left-hand side, when written in matrix form, lie in the leading diagonal. Equation(s) (11) are then solved through re-writing:

$$\ddot{w}^{(n+1)}_{ij} = \frac{F_{ij} - (\rho/2\pi\rho_m h) \sum_{m=1, m\neq i}^{M-1} \sum_{n=1, n\neq j}^{N-1} I^{\Phi}_{ijmn} \ddot{w}^{(n)}_{mn}}{1 + (\rho/2\pi\rho_m h) I^{\Phi}_{ijij}} \tag{12}$$

where (n) is the iteration number for this procedure. At each iteration (12) is used for a sweep through the panel-elements. As they become available in the course of this sweep, updated values of $\ddot{w}^{(n)}_{m,n}$ (i.e. with $(n + 1)$ replacing (n) on the right-hand side) are used in the summation seen above. The above procedure may be recognized as a Gauss–Seidel method with pivoting. It is noted that, for each value of ij, the right-hand side of (12) can be calculated in a single parallel operation. Used in tandem with the memory-saving technique described above, the procedure only utilises arrays that match the basic array size of the DAP. Of course, the savings in storage that this method achieves are bought by increased computational time when compared to the direct method of solving (10) using matrix inversion. However, for large mesh sizes the use of the direct method would require external storage of the inverted matrix and the repeated conversion of data type between host and DAP entry program would result in massive increases to the program run time. Lastly, it is noted that the use of an internal mesh does not fully capture the hydrodynamic inertia of the dynamic system since the contribution of the set of 'half panel-elements' adjacent to the compliant-panel edges has been neglected. When this alternative method is appropriately used (for the larger mesh sizes), this error becomes negligible.

RESULTS

In order to investigate the behaviour of the interactive wall/flow model, an initial perturbation from the equilibrium position is required. This might take the form of a localised disturbance of the wall position, an isolated pressure pulse or a pressure pulse travelling in the flow. For the purposes of testing the model, we will initiate the wall motion by imposing a deflection and releasing the wall at time $t = 0$. A pressure-pulse excitation is included in the further results which follow the testing.

Model testing

Before undertaking any 'numerical experiments', it is necessary to validate the response predictions of the present model. Comparison is made with the semi-analytical modal study of Lucey and Carpenter[23] which was, in part, summarized above under the heading Mathematical Model. Thus, we have used the spatially dependent part of (2) to define an initial displacement. Through-out this sub-section the data used has that: $h = 0.01$ m, $B = 4904$ Nm, $K_E = 0$, $\rho_m = 2600\,\text{kg/m}^3$ and $\rho = 1000\,\text{kg/m}^3$. Furthermore, wall damping is absent.

Figure 3 shows the response of a panel with dimensions, $a = b = 1.0$ m, at different flow speeds after an initial deflection given by (2) using only the fundamental mode ($k = l = 1$) and with $A_{11} = 0.002$ m. The time-steps are of size 10^{-4} sec and approximately six iterations are required before convergence is achieved at each time-step. *Figures 3a, 3b* and *3c* respectively show the deflection of the panel mid-point, w_{55}, with the passage of time for the flow speeds $U_\infty = 10$, 40 and 50 m/sec. *Figures 3d* ($U_\infty = 10$ m/sec), *3e* ($U_\infty = 40$ m/sec) and *3f* with *3g* ($U_\infty = 50$ m/sec) are 'snapshots' of the complete compliant panel at the indicated times, t, after the initial perturbation. At 10 m/sec sub-critical oscillatory behaviour is seen whilst at the higher, post-critical flow speeds, divergence instability is manifest. It is noted that divergence takes the form of a downstream-travelling wave rather than the truly static instability predicted by standing-wave methods[18–20,23]. In *Figure 4* the sub-critical angular frequencies of oscillation (ω_r) and post-critical growth rates ($-\omega_i$) obtained using the present model are compared with those found using a single (fundamental) mode analysis. This Figure also gives an indication of the necessary resolution of wall disturbances in the numerical model in order to determine the divergence-onset flow speed accurately. It must be remarked that this comparison of methods is not entirely appropriate since the standing-wave model has been constrained to a single mode. Whilst the present method reproduces essentially single-mode behaviour at relatively low flow speeds (*Figures 3a* and *3d*) and exactly at divergence onset, it can be seen from *Figures 3e, 3f* and *3g* that other modes have entered the solution in a natural manner. It is thus immediately obvious that the present method provides a substantial improvement upon the standing-wave methods for which the modes present must be prescribed in advance.

The behaviour of a panel with dimensions, $a = 1.0$ m and $b = 0.5$ m, close to the critical flow speed is seen in *Figure 5*. In these cases, an appropriate time-step has size 10^{-5} sec. For this aspect ratio, a modal analysis predicts that the most dangerous mode (that which has the lowest divergence-onset flow speed) has $k = 2$ and $l = 1$. This has been verified by the present method. *Figures 5a, 5b* and *5c*, all at 90 m/sec show sub-critical behaviour with upstream wave travel whilst *Figures 5d, 5e* and *5f*, all at 100 m/sec illustrate divergence instability as a downstream-travelling wave. In reality, damping would quickly attenuate the sub-critical upstream waves and slightly reduce the growth rate of the divergence waves.

Further results

The preceding sub-section has shown that, once a certain divergence-onset flow speed is exceeded, the instability does not occur as the simple amplification of a fixed displacement field which has been suggested by the standing-wave methods of prediction[18–20,23]. However, these semi-analytical methods and the present method do give the same onset flow speed. The present numerical simulation shows the travelling-wave nature of divergence instability. A clear demonstration of this is presented in *Figures 6* and *7*. The material properties of the compliant wall used for these results are akin to those used in the original Kramer walls discussed in Reference 1: $B = 3.56 \times 10^{-4}$ Nm, $K_E = 3.5 \times 10^5\,\text{N/m}^3$, $\rho_m = 952\,\text{kg/m}^3$ with dimensions

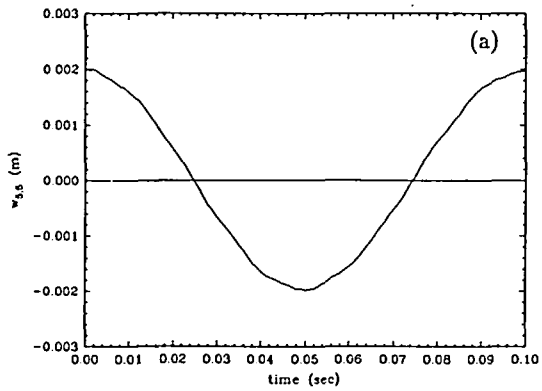

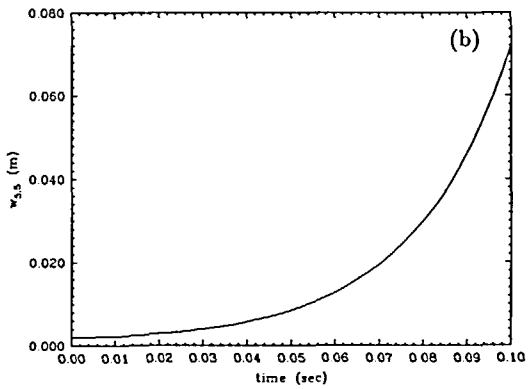

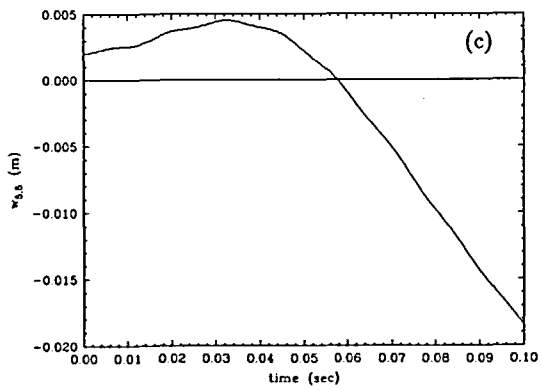

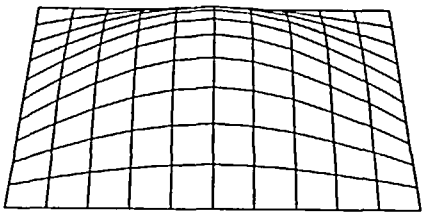

(d) $t = 0.1$ s

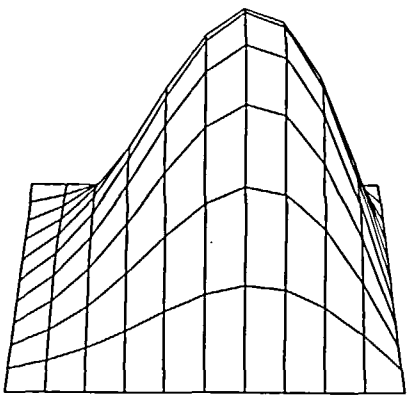

(e) $t = 0.1$ s

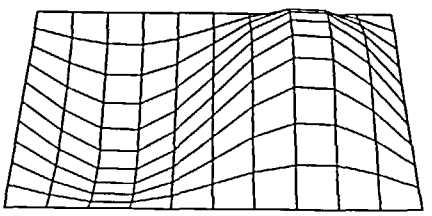

(f) $t = 0.05$ s

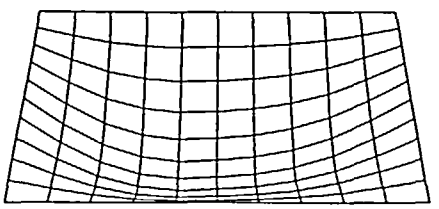

(g) $t = 0.1$ s

Figure 3 Wall response at different flow speeds. Deflection of panel mid-point, w_{55}, *vs.* time for: (a) $U_\infty = 10$ m/sec, (b) $U_\infty = 40$ m/sec, (c) $U_\infty = 50$ m/sec. 'Snapshots' of the displaced wall with the vertical deflection scaled by a factor, SF (the flow is from left to right): (d) $U_\infty = 10$ m/sec, $SF = 1000$, $t = 0.1$ sec, (e) $U_\infty = 40$ m/sec, $SF = 100$, $t = 0.1$ sec, (f) $U_\infty = 50$ m/sec, $SF = 100$, $t = 0.05$ sec, (g) $U_\infty = 50$ m/sec, $SF = 100$, $t = 0.1$ sec. Data used: $h = 0.01$ m, $B = 4094$ Nm, $K_E = 2600$ kg/m^3, $d = 0$ and $\rho = 1000$ kg/m^3. $a = b = 1.0$ m

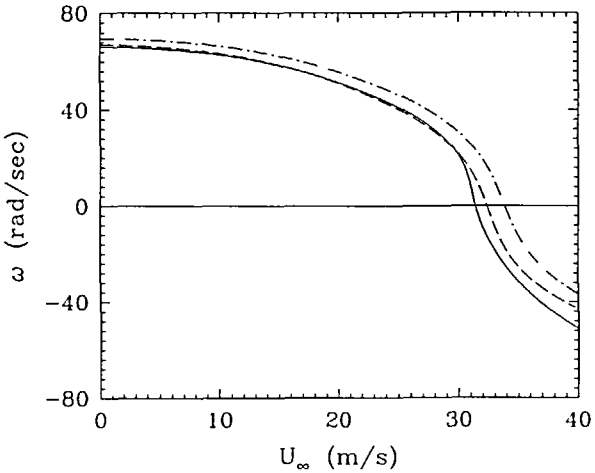

Figure 4 Complex angular frequency, $\omega\ (= \omega_r + i\omega_i)$, *vs.* free-stream flow speed for a fundamental-mode disturbance. ω_r and ω_i are respectively plotted on the positive and negative axes. ——, modal analysis (from Reference 23); – –, present method, 10 × 10 mesh; –·–, present method, 5 × 5 mesh. Data as for *Figure 2*

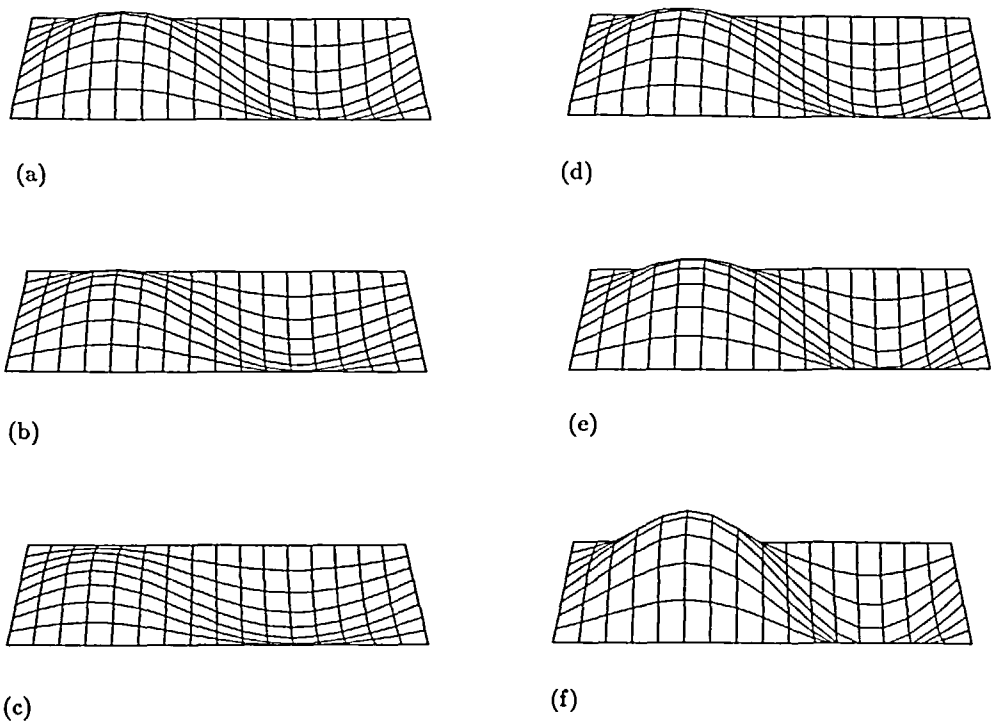

Figure 5 Wall response at sub-critical (left column) and post-critical (right column) flow speeds. The flow is from left to right. $U_\infty = 90$ m/sec: (a) $t = 0$ sec, (b) $t = 0.005$ sec, (c) $t = 0.010$ sec. $U_\infty = 100$ m/sec, (d) $t = 0$ sec, (e) $t = 0.005$ sec, (f) $t = 0.010$ sec. Data as for *Figure 2* except that $a = 1.0$ m and $b = 0.5$ m. $SF = 100$ throughout

$a = b = 0.10$ m and $h = 2$ mm. The fluid density, ρ, is 1000 kg/m^3. Wall damping is absent; this point is emphasized because a travelling-wave hydroelastic analysis of an infinitely long compliant wall suggests that wall damping is essential for the realization of divergence instability.

Shown in *Figure 6a* is the initial deflection (at $t = 0$) imposed upon the compliant panel which has been discretized using a 30 × 30 mesh. The flow speed, U_∞, is parallel to the x-direction. A vertical scale factor of 3000 has been applied in this and all the following 'snapshot' results presented. At a sub-critical flow speed, $U_\infty = 2$ m/sec, a typical evolution of the disturbance is represented by *Figures 6b* and *6c* plotted at $t = 0.006$ sec and $t = 0.012$ sec respectively. The deformation initially remains three-dimensional with flexural waves propagating outwards from the central disturbance. Note the distortion of these waves due to the hydrodynamic effects: the phase speed of the downstream-travelling wavefront is greater than its upstream-travelling

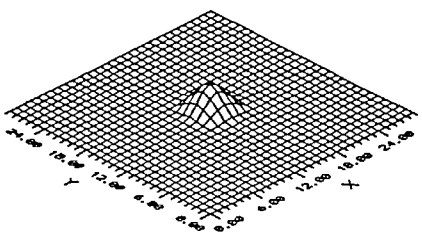

(a) $t = 0$ s

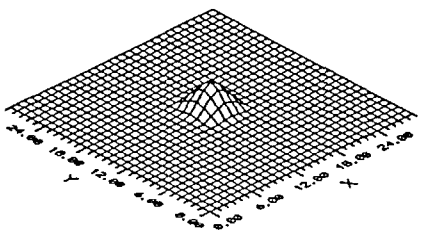

(d) $t = 0$ s

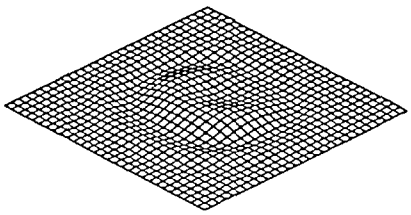

(b) $t = 0.006$ s

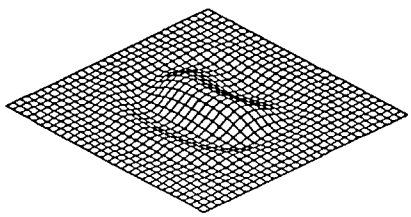

(e) $t = 0.006$ s

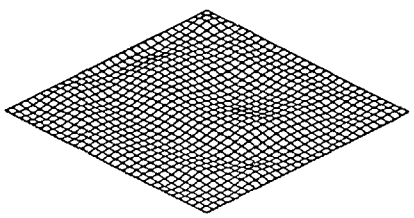

(c) $t = 0.012$ s

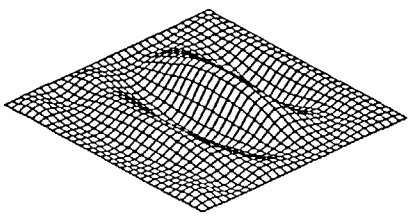

(f) $t = 0.012$ s

Figure 6 Response at sub-critical (left column) and post-critical (right column) for a Kramer-type wall. The flow is in the positive x-direction. $U_\infty = 2$ m/sec: (a) $t = 0$ sec, (b) $t = 0.006$ sec, (c) $t = 0.012$ sec. $U_\infty = 3$ m/sec: (d) $t = 0$ sec, (e) $t = 0.006$ sec, (f) $t = 0.012$ sec. Data used: $h = 0.002$ m, $B = 3.56 \times 10^{-4}$ Nm, $K_E = 3.5 \times 10^5$ N/m^3, $\rho_m = 952$ kg/m^3, $d = 0$ and $\rho = 1000$ kg/m^3. $a = b = 0.1$ m. $SF = 3000$ throughout

counterpart. At the later time, there is evidence of wave-reflection at the panel edges. Ultimately, the downstream-travelling waves come to dominate the wall response.

The system behaviour at a post-critical flow speed, $U_\infty = 3$ m/sec after the initial deflection (*Figure 6d*) is depicted in *Figures 6e* ($t = 0.006$ sec) and *6f* ($t = 0.012$ sec). Divergence instability is found. In contrast to the sub-critical behaviour, the panel response is dominated by quasi-two-dimensional effects, the instability occurring as a slow downstream-travelling wave. It should also be noted that amplitude growth is found at locations upstream of the initial excitation—this feature strongly suggests that divergence is an absolute instability despite the manifest waves having a positive phase speed. The form of the divergence waves is further illustrated in *Figure 7*, which employs the results at $U_\infty = 3$ m/sec and $t = 0.012$ sec. *Figure 7a* is a side view of the unstable wave whilst *Figure 7b* is a contour plot of the compliant-panel topography from which the instability wavelength can readily be deduced. Other results, not presented here, have investigated the dependence of divergence upon wall parameters. These essentially reproduce the findings of Garrad and Carpenter[20] and Lucey and Carpenter[23]. For example, increasing the wall stiffness through either B or K_E raises the onset flow speed of the instability and, at a given unstable flow speed, an increase to $B(K_E)$ leads to a decrease (increase) in the wavelength of the divergence wave.

The present numerical method thus evinces good qualitative agreement with the experimental findings of Hansen and Hunsten[12,13] and Gad-el-Hak, Blackwelder and Riley[14]; divergence is a slow downstream-travelling wave with a wavelength dependent upon the wall properties. However, it has been suggested[14,25] that the presence of wall damping is essential for divergence to exist. This contention finds support in travelling-wave analyses of infinitely long compliant walls[1,17,26,27]. However, the results discussed above show divergence in the absence of damping. In two-dimensional simulations, Lucey and Carpenter[16] have explained that, where divergence is concerned, the leading and trailing edges generate the destabilizing effect played by damping in travelling-wave analyses so allowing damping to revert to its more orthodox role of attenuation. *Figures 8a* and *8b* demonstrate that this also holds true for the present extension into three-dimensions. These Figures show the way that the wall energy changes with time for flow speeds beneath (*Figure 8a*) and above (*Figure 8b*) divergence-onset and pertain to the sequences seen in *Figures 6*. The wall energy, E_W, comprises strain and kinetic energies and is evaluated

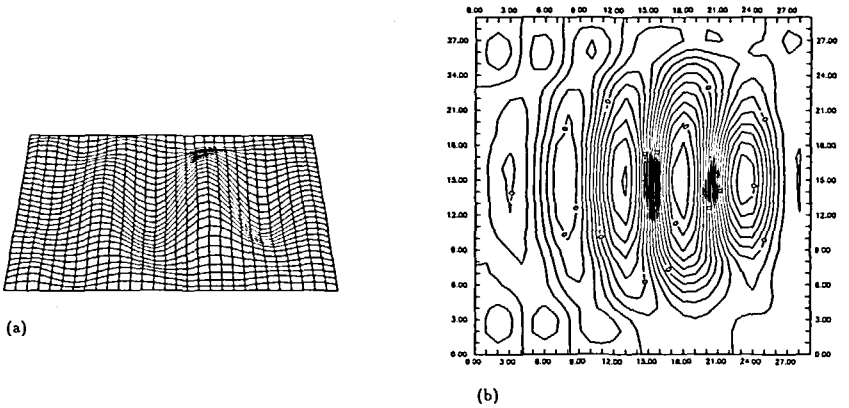

Figure 7 Divergence waves on the compliant panel: (a) side view ($SF = 3000$), (b) contour plot (contour spacing is 10^{-4} m). The flow is from left to right. Data as for *Figure 6f*

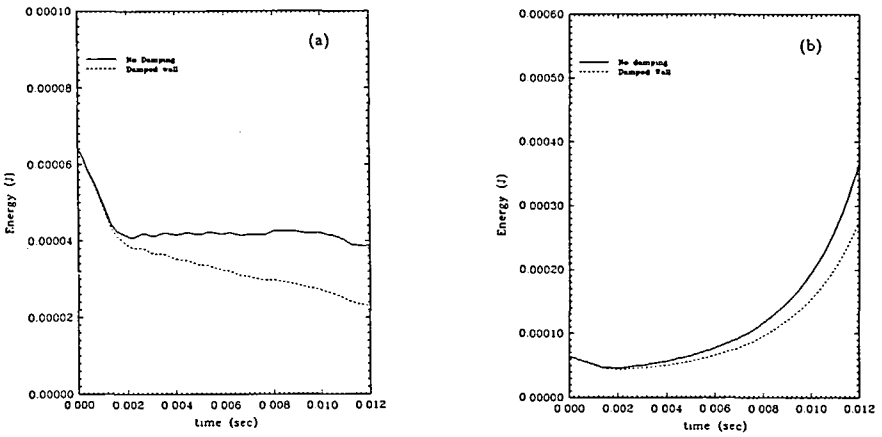

Figure 8 Variation of total wall energy with time for the runs presented in *Figure 6* and equivalent runs with wall damping, d, included. (a) $U_\infty = 2$ m/sec: ——, $d = 0$; – – –, $d = 276$ N sec/m^3. (b) $U_\infty = 3$ m/sec; ——, $d = 0$; – – –, $d = 276$ N sec/m^3

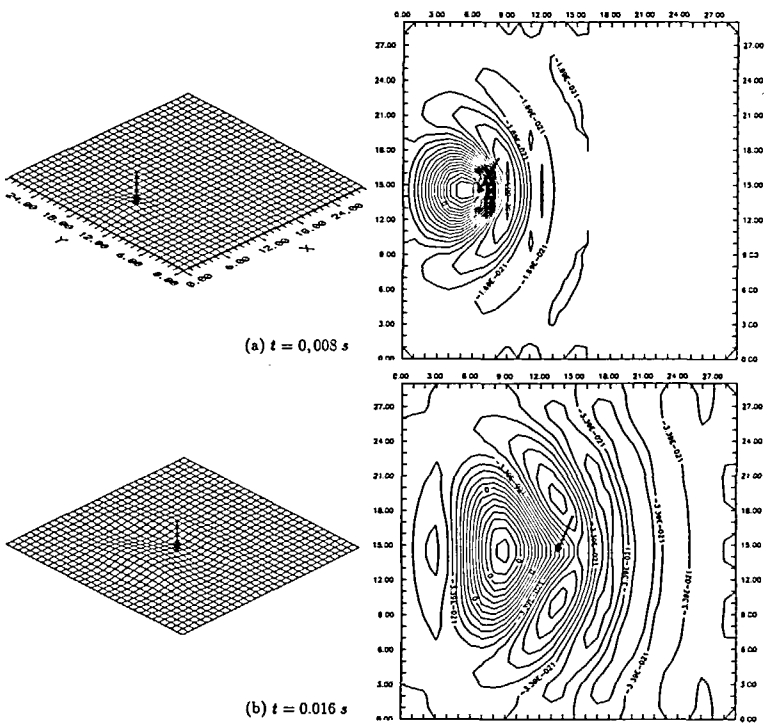

Figure 9 'Snapshots' and associated contour plots of wall response whilst (and after) a point pressure pulse travels over the compliant panel, showing the development of divergence waves. $U_\infty = 3$ m/sec. Wall data as for *Figure 6*. The pulse is generated by a disturbance $0.1U_\infty$ from the mean flow. The flow is in the positive x-direction. (a) $t = 0.008$ sec, (b) $t = 0.016$ sec, (c) $t = 0.024$ sec, (d) $t = 0.032$ sec, (e) $t = 0.040$ sec. The arrow marks the location of the pressure pulse at the time of plotting

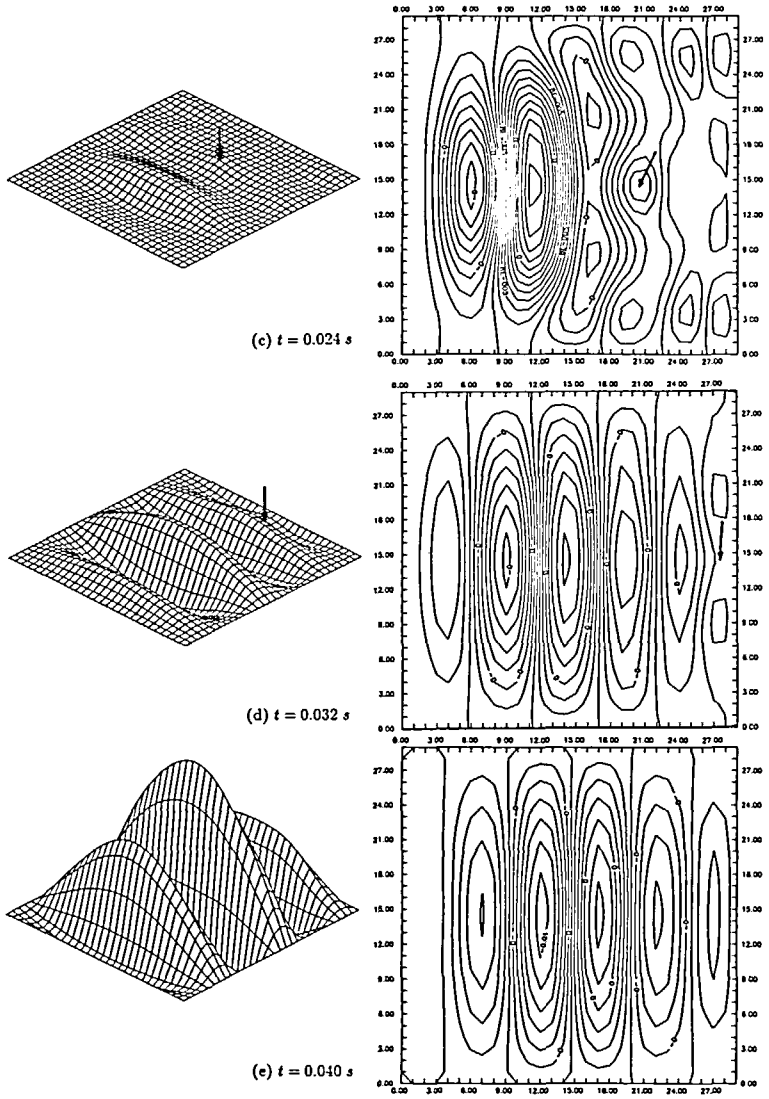

Figure 9 continued

through the following:

$$E_W = \sum_{i=1}^{M-1} \sum_{j=1}^{N-1} \{Bw_{ij}\nabla^2\nabla^2 w_{ij} + K_E w_{ij}^2 + \rho_m h\dot{w}_{ij}^2\}\frac{\delta x \delta y}{2} \tag{13}$$

At the sub-critical flow speed, the wall energy is seen first to drop before the system arrives at a form of neutral stability. Damping dissipates the wall energy, eventually eliminating the disturbance. At the post-critical flow speed, instability is clearly recorded by the rapid increase in wall energy. Damping serves only marginally to counter the rate of energy transfer from the flow into the wall. Note the initial drop in wall energy; this occurs at times during which the

divergence wave is being formed. Damping does not alter the critical flow speed since exactly at onset wall and fluid stiffnesses are exactly in balance resulting in no motion.

Finally, the wall response to a pressure pulse is investigated. The above form of initial excitation—imposing a 'bump' on the compliant panel—is somewhat artificial. Here a point pressure pulse is allowed to travel, at the flow speed, over the compliant panel having first appeared at the leading edge at $t = 0$ sec. The pressure pulse is modelled as a perturbation from the free stream flow speed at the pulse location, the boundary-element method being adjusted to accommodate the consequent spatially-dependent applied flow. Run at a post-critical flow speed, $U_\infty = 3$ m/sec, *Figure 9* shows a succession of both 'snapshots' and contour plots of the wall. The position of the pulse at the time of plotting is included for those cases in which the pulse is over the compliant panel. This set of Figures illustrates the development of the predominantly two-dimensional divergence wave from the three dimensional flexural waves which spread out from the initiating source of energy.

CONCLUSIONS

A method has been developed to simulate numerically the three-dimensional interaction of a finite compliant panel with an unsteady potential flow. A spring-backed flexible plate has been used for the compliant-wall model; however, the general method—coupling a boundary-element flow solution to a dynamic wall solution—can also be used to investigate the behaviour of other types of compliant wall, e.g. single- or multi-layer viscoelastic continua, provided that suitable wall solutions are available. Parallel computing has been shown to be applicable to each aspect (fluid and solid dynamics, solution of the coupled system) of the present method having couched the problem so as fully to exploit the architecture of the array processor.

The method has been tested against the predictions of a modal stability analysis and shown to give corresponding instability-onset flow speeds. The numerical simulation improves on previous standing-wave predictions; divergence instability is now seen to take the form of slow downstream-travelling waves which are essentially two-dimensional in character. As time passes, these waves come to occupy all regions of the compliant panel, even those locations upstream of the point of initial excitation. This description agrees with experimental findings. At sub-critical speeds, the response is primarily three-dimensional with flexural waves transmitting energy outwards from the point of excitation. Wall damping has been shown to attenuate the sub-critical response but only slightly reduce the growth rate of divergence instability. The critical flow speed for divergence onset is indifferent to wall damping.

Although we have developed a linear wall/flow model in this paper, the general boundary-element method, could be used to investigate divergence instability for non-linear disturbances. This would necessitate the inclusion of non-linear terms in the wall mechanics which principally arise from in-plane stretching of the plate. A further, and perhaps more interesting, development would be to incorporate a boundary layer into the present simulations.

ACKNOWLEDGEMENTS

This work is part of a research programme at the University of Warwick which is supported by the Ministry of Defence (Procurement Executive).

REFERENCES

1 Carpenter, P. W. and Garrad, A. D. The hydrodynamic stability of flows over Kramer-type compliant surfaces. Part 1. Tollmien–Schlichting instabilities, *J. Fluid Mech.*, **155**, 465–510 (1985)

2 Yeo, K. S. The stability of boundary-layer flow over single- and multi-layer viscoelastic walls, *J. Fluid Mech.*, **196**, 359–408 (1988)
3 Yeo, K. S. The hydrodynamic stability of boundary-layer flow over a class of anisotropic compliant walls, *J. Fluid Mech.*, **220**, 125–160 (1990)
4 Carpenter, P. W. and Morris, P. J. The effects of anisotropic wall compliance on boundary-layer stability and transition, *J. Fluid Mech.*, **218**, 171–223 (1990)
5 Daniel, A. P., Gaster, M. and Willis, G. J. K. Boundary-layer stability on compliant surfaces, *Report British Maritime Technology Ltd* (1987)
6 Gaster, M. Is the dolphin a red herring? *IUTAM Symp. Turbul. Manag. Relamin. Bangalore*, (Eds. Liepmann, H. W. and Narasimha, R.), Springer-Verlag, New York, pp. 285–304 (1987)
7 Willis, G. J. K. Hydrodynamic stability of boundary layers over compliant surfaces, *PhD Thesis*, University of Exeter (1986)
8 Carpenter, P. W. The optimization of multi-panel compliant walls for delay of laminar-turbulent transition, *AIAA Paper 91-1772* (1991)
9 Carpenter, P. W., Lucey, A. D. and Dixon, A. E. The optimisation of compliant walls for drag reduction, *Recent Developments in Turbulence Management*, (Ed. K.-S. Choi), Kluwer Academic Publishers, Dordrecht, pp. 195–221 (1991)
10 Lucey, A. D., Carpenter, P. W. and Dixon, A. E. The role of wall instabilities in boundary-layer transition over compliant walls, in *Proc. Bound. Layer Transit. Control Conf. Cambridge*, [*Royal Aero Soc.*, 35.1–35.10 (1991)]
11 Carpenter, P. W. Status of transition delay using compliant walls, *Viscous Drag Reduction in Boundary Layers*, (Eds. Bushnell, D. M. and Hefner, J. M.), Vol. 23 of *Progr. Astronaut. Aeronaut.* AIAA, Washington, DC, pp. 79–113 (1990)
12 Hansen, R. J. and Hunsten, D. L. An experimental study of turbulent flows over compliant surfaces. *J. Sound Vib.*, **34**, 297–308 (1974)
13 Hansen, R. J. and Hunsten, D. L. Fluid-property effects on flow-generated waves on a compliant surface, *J. Fluid Mech.*, **133**, 161–177 (1983)
14 Gad-el-Hak, M., Blackwelder, R. F. and Riley, J. F. On the interaction of compliant coatings with boundary-layer flows, *J. Fluid Mech.*, **140**, 257–280 (1984)
15 Carpenter, P. W. and Garrad, A. D. The hydrodynamic stability of flows over Kramer-type compliant surfaces. Part 2. Flow-induced surface instabilities, *J. Fluid Mech.*, **170**, 465–510 (1985)
16 Lucey, A. D. and Carpenter, P. W. A numerical simulation of the interaction of compliant wall and inviscid flow, *J. Fluid Mech.*, **234**, 121–146 (1992)
17 Dugundji, J., Dowell, E. H. and Perkin, B. Subsonic flutter of panels on a continuous elastic foundation, *AIAA J.*, **1**, 1146–1154 (1963)
18 Weaver, D. S. and Unny, T. S. The hydroelastic stability of a flat plate, *J. Appl. Mech.*, **37**, 823–827 (1971)
19 Ellen, C. H. The stability of simply supported rectangular surfaces in uniform subsonic flow, *J. Appl. Mech.*, **40**, 68–72 (1973)
20 Garrad, A. D. and Carpenter, P. W. A theoretical investigation of flow-induced instabilities in compliant coatings, *J. Sound Vib.*, **84**, 483–500 (1982)
21 Kramer, M. O. Boundary-layer stabilization by distributed damping, *J. Am. Soc. Naval Eng.*, **72**, 25–33; *J. Aero/Space Sci.*, **27**, 69 (1960)
22 Dowell, E. H. *Aeroelasticity of plates and shells*, Noordhoff, Dordrecht (1975)
23 Lucey, A. D. and Carpenter, P. W. The hydroelastic stability of three-dimensional disturbances of a finite compliant panel, *J. Sound Vib.*, (to appear) (1993)
24 Hess, J. L. and Smith, A. M. O. Calculation of potential flow about arbitrary bodies, Vol. 8 of *Progr. Aeronaut. Sci.*, Pergamon Press, New York, pp. 1–138 (1966)
25 Gad-el-Hak, M. The response of elastic and viscoelastic surfaces to a turbulent boundary layer, *J. Appl. Mech.*, **53**, 206–212 (1985)
26 Landahl, M. T. On the stability of a laminar incompressible boundary layer over a flexible surface, *J. Fluid Mech.*, **13**, 602–632 (1962)
27 Benjamin, T. B. The threefold classification of unstable disturbances in flexible surfaces bounding inviscid flows, *J. Fluid Mech.*, **16**, 436–450 (1963)